mater.scichina.com link.springer.com

Published online 23 August 2022 | https://doi.org/10.1007/s40843-022-2142-1
Sci China Mater 2023, 66(1): 51–60

N-doped $Ti_3C_2T_x$ MXene sheet-coated SiO_x to boost lithium storage for lithium-ion batteries

Kaiyuan Zhang[1], Dan Zhao[2], Zhao Qian[2*], Xin Gu[3*], Jian Yang[1*] and Yitai Qian[1,4]

ABSTRACT **Constructing SiO_x-based composite materials with fast reaction kinetics and high stability is crucial but challenging for high-performance lithium-ion batteries. Herein, we developed the N-doped $Ti_3C_2T_x$ MXene ultrathin sheet (NTS)-coupled SiO_x nanoparticles using a melamine-assisted ball milling and annealing procedure. The principle of melamine in exfoliating MXene was demonstrated by contrast experiments and theoretical calculations. The strong interfacial interactions between SiO_x and the NTS (Si–O–Ti bond) can effectively enhance the electron transfer and ensure electrode stability. Moreover, the NTS with rich surface groups endowed the composite with a pseudocapacitive behavior, beneficial for fast lithium storage. As a result, the composite delivered a long lifespan (~700 mA h g^{-1} over 800 cycles at 1.0 A g^{-1}) and a superior rate performance (596.4 mA h g^{-1} at 5 A g^{-1}). More importantly, the composite in half and full cells exhibited high areal capacity and good cycling stability at high mass loadings, revealing a promising application prospect.**

Keywords: lithium-ion batteries, SiO_x-based anode materials, N-doped $Ti_3C_2T_x$ MXene nanosheets, ball milling exfoliation, adsorption energy

INTRODUCTION

Silicon suboxide (SiO_x, $0 < x < 2$) has shown great potential in high-energy lithium-ion batteries (LIBs) for its high theoretical capacity (2200–3580 mA h g^{-1}) and relatively stable cycling performance [1–3]. Unlike Si, the volume change in SiO_x during the charge/discharge process can be inhibited to some extent by *in-situ*-generated lithium oxide (Li_2O) and lithium silicate (Li_4SiO_4) [4–6]. Although the presence of oxygen sacrifices a part of the specific capacity, the cycling stability and economy of SiO_x are superior to those of Si [7–9]. However, SiO_x still faces critical challenges, such as large volume expansion (~200%) [10], low electrical conductivity [11], and the formation of unstable solid electrolyte interphase (SEI) film [12], which usually causes electrode pulverization and results in a rapid capacity decay [13–15]. Researchers attempted to remedy these demerits by compositing SiO_x with a highly conductive and flexible carbon for lithium storage enhancements [16], including SiO_x/carbon nanotubes [17], SiO_x/graphene [18], and SiO_x/graphite [19]. Nevertheless, these carbon materials show weak interfacial interaction with SiO_x because of their sp^2 carbon-bounded surface with fewer polar groups, which restricts the electron transfer between SiO_x and carbon in the composite [20]. Hence, developing new types of materials for compositing with SiO_x is crucial but challenging.

Titanium carbide ($Ti_3C_2T_x$) MXene, a new two-dimensional (2D) material introduced by Gogotsi and his collaborators [21], exhibits a good transmission rate and low diffusion barrier for Li-ion, and it is widely applied in the field of energy storage [22–29]. Given the rich terminal groups and abundant redox reactions on the surface of $Ti_3C_2T_x$ MXene, it easily combines with other materials and exhibits significant pseudocapacitive contributions. As for the Si anode, Gogotsi's group [30] dispersed $Ti_3C_2T_x$ MXene in an organic solution to prepare a viscous slurry, and they combined nano-Si tightly with the current collector using the viscosity of this slurry. Song's group [31] used hydrothermal and freeze-drying methods to embed nano-Si into a 3D conductive network composed of $Ti_3C_2T_x$ MXene to obtain a high-performance electrode. Yin's group [32] employed MXene as a conductive substrate during a low-temperature molten salt process to reduce silica to Si and successfully combined 0D Si with 2D layered MXene, achieving an excellent electrochemical performance. However, these efforts on Si/MXene combination still have some defects. For instance, a weaker interaction force has been observed between Si and MXene as these synthetic routes are based on simple physical mixing. Raw materials, such as porous silicon or nano-Si (<100 nm), usually lead to low tap density and secondary agglomeration of nanoparticles (NPs) because the nonporous characteristic of MXene causes difficulty in providing extra space for the huge volume change of Si [33]. Many efforts have been exerted, but given the differences between 0D nano-Si and 2D layered MXene in morphology, blending and compositing them tightly are still challenging.

In this work, a scalable preparation strategy comprising ball milling and annealing was proposed to construct an ultrathin N-doped $Ti_3C_2T_x$ MXene sheet-coated SiO_x composite (SiO_x@NTS) as an anode material for LIBs. Melamine was introduced as the exfoliation agent for peeling multilayered MXene during ball

[1] Key Laboratory of Colloid and Interface Chemistry, Ministry of Education, School of Chemistry and Chemical Engineering, Shandong University, Jinan 250100, China
[2] Key Laboratory for Liquid-Solid Structural Evolution and Processing of Materials, Ministry of Education, School of Materials Science and Engineering, Shandong University, Jinan 250061, China
[3] College of New Energy, State Key Laboratory of Heavy Oil Processing, China University of Petroleum (East China), Qingdao 266580, China
[4] Hefei National Laboratory for Physical Science at Microscale, Department of Chemistry, University of Science and Technology of China, Hefei 230026, China
[*] Corresponding authors (emails: qianzhao@sdu.edu.cn (Qian Z); guxin@upc.edu.cn (Gu X); yangjian@sdu.edu.cn (Yang J))

milling and as the nitrogen source for the preparation of N-doped $Ti_3C_2T_x$ MXene during annealing. The SiO_x@NTS showed several unique merits in improving the Li storage performance, i.e., a strong interaction force between the NTS shell and SiO_x core to accelerate the interfacial electron transfer and ensure structural stability. In addition, extrinsic defects induced the high electrical conductivity and robust flexibility of $Ti_3C_2T_x$ MXene to support the capacity output of SiO_x. As a result, the SiO_x@NTS showed enhanced electrochemical performances in Li-ion half and full cells and a high areal capacity under heavy mass loading.

EXPERIMENTAL SECTION

Material synthesis

Preparation of $Ti_3C_2T_x$ MXene: $Ti_3C_2T_x$ MXene was synthesized by etching Ti_3AlC_2 MAX with HF solution. Typically, 1.0 g of Ti_3AlC_2 (400 mesh, purchased from 11 Technology Co., Ltd.) was slowly added to the HF solution (40%). After stirring at 35°C for 24 h, the product was collected by centrifugation at 10,000 r min^{-1} for 3 min, washed with deionized water and absolute ethanol several times, and dried at 60°C.

Preparation of SiO_x@NTS, SiO_x/T, and NTS: First, 35 mg of the as-prepared $Ti_3C_2T_x$ MXene, 80 mg of the commercial micro SiO, and 350 mg of melamine (AR, purchased from Sinopharm Chemical Reagent Co., Ltd.) were placed in an agate jar. After the addition of 10 g of agate balls, the jar was sealed in a glove box filled with argon gas and ball milled for 48 h at a speed of 600 r min^{-1}. Then, the ball-milled powder was annealed at 900°C for 3 h, with a heating rate of 5°C min^{-1}. Finally, the product was dispersed in 1 mol L^{-1} NaOH solution to remove impurities. After reacting for 3 h, the SiO_x@NTS was collected by a vacuum system, washed with deionized water and absolute ethanol several times, and dried at 60°C for 9 h. For comparison, SiO_x/T was prepared using the same synthetic procedure but without adding melamine. The NTS was synthesized by treating the SiO_x@NTS with HF solution for 3 h.

Electrochemical measurements

For half cells, the active material, acetylene black, and sodium alginate at a weight ratio of 7:2:1 were mixed and dispersed in deionized water to prepare a slurry. Then, the slurry was pasted on a Cu foil, followed by drying at 60°C overnight. The mass loading of the active material in the electrode was 1.2 mg cm^{-2}. To evaluate the areal capacity, we controlled the mass loading at 0.78–3.5 mg cm^{-2}. The working electrode, Celgard 2400 separator, and counter electrode (Li metal) were assembled into CR2025 coin cells in a glove box filled with Ar gas. Cyclic voltammetry (CV) and electrochemical impedance spectroscopy (EIS) were tested on a Lanlike electrochemical workstation (LK2005A, China) over a voltage range of 0.01–1.5 V and a Metrohm electrochemical workstation (Autolab 302N, Switzerland) between 100 kHz and 0.1 Hz, respectively. For full cells, the cathode slurry was prepared by 80 wt% commercial $LiNi_{0.6}Co_{0.2}Mn_{0.2}O_2$ (NCM622), 10 wt% acetylene black, and 10 wt% polyvinylidene fluoride in *N*-methyl pyrrolidone, cast onto Al foil, and dried in a vacuum oven. Before assembling SiO_x@NTS//NCM622 full cells in CR2025-type coin cells, the anode was first discharged and charged in half cells for three cycles. The electrolyte for half and full cells was 1.0 mol L^{-1} $LiPF_6$ in a mixture of ethylene carbonate/dimethyl carbonate (*v*/*v*, 1:1) containing 7% fluoroethylene carbonate. The electrochemical performances of the half and full cells were evaluated by the galvanostatic charge and discharge processes.

Material characterization

Scanning electron microscopy (SEM) images were acquired on a field-emission scanning electron microscope (Zeiss Gemini 300, Germany). Transmission electron microscopy (TEM) images were obtained on a transmission electron microscope (JEOL JEM 1011, Japan). High-resolution TEM (HRTEM) images, high-angle annular dark-field (HAADF) images, and element mapping images were acquired on a transmission electron microscope (FEI TalosF200x, USA). X-ray diffraction (XRD), Raman spectra, and X-ray photoelectron spectroscopy (XPS) results were obtained using an X-ray diffractometer (Bruke D8 advance, Germany), MicroRaman spectrometer (HORIBA JYHR800, Japan), and X-ray photoelectron spectrometer (Thermo Fischer ESCALAB 250, USA), respectively. The N_2 sorption isotherms and calculated Brunauer-Emmett-Teller (BET) surface area were studied using a gas sorption analyzer (Micromeritics ASAP 2020, USA). The infrared spectrum was obtained from a Fourier transform infrared spectroscopy (FTIR) spectrometer (Bruker Tensor 27, Germany). Atomic force microscopy (AFM) images were recorded on a NanoScope V controlled microscope (Bruker Bioscope Resolve, Germany).

First-principle calculations

The detailed density functional theory (DFT) calculation steps can be acquired in Supplementary information.

RESULTS AND DISCUSSION

Fig. 1a describes the synthetic process for SiO_x@NTS, which includes ball milling and annealing steps. In the first high-energy ball milling process, multilayer $Ti_3C_2T_x$ MXene was mechanically exfoliated into $Ti_3C_2T_x$ MXene sheets (TS), where melamine acted as the exfoliation agent. Meanwhile, micron-sized SiO was ground into SiO NPs. As the grinding continued, these different components were well distributed to form the SiO NP/TS/melamine mixture. In the next annealing process, melamine acted as the N source to promote nitrogen doping and the crumpling of TS, thus ensuring its coating on the surface of SiO_x [34]. SiO_x/multilayer $Ti_3C_2T_x$ MXene (SiO_x/T) was synthesized as the benchmark to illustrate the benefits of NTSs. The structural models of TS and NTS are presented in the red boxes in Fig. 1a, in which blue, brown, light purple, and pink balls represent Ti, C, N, and H atoms, respectively. The morphologies of the multilayered $Ti_3C_2T_x$ MXene, SiO_x@NTS, and SiO_x/T were characterized by SEM and TEM images (Fig. 1 and Figs S1–S6). The multilayer $Ti_3C_2T_x$ MXene showed an accordion-like structure with a block thickness of about 10 μm (Fig. 1b and Fig. S1), confirming its successful exfoliation from Ti_3AlC_2 MAX [35]. The SiO_x@NTS consisted of well-dispersed SiO_x NPs with sizes ranging from 200 to 800 nm, together with numerous nanosheets surrounding the NPs (Fig. 1c and Fig. S2). Furthermore, from the TEM and HRTEM images, the SiO_x NPs were closely covered by the NTS (Fig. 1d, e and Fig. S3), suggesting a typical core-shell construction. The contour of the SiO_x@NTS constructed by Si, O, C, Ti, and N and nitrogen doping in NTS were further proven by scanning TEM (STEM) image and the corresponding energy dispersive spectrum (EDS) mapping images (Fig. 1f and Fig. S4). The difference in the

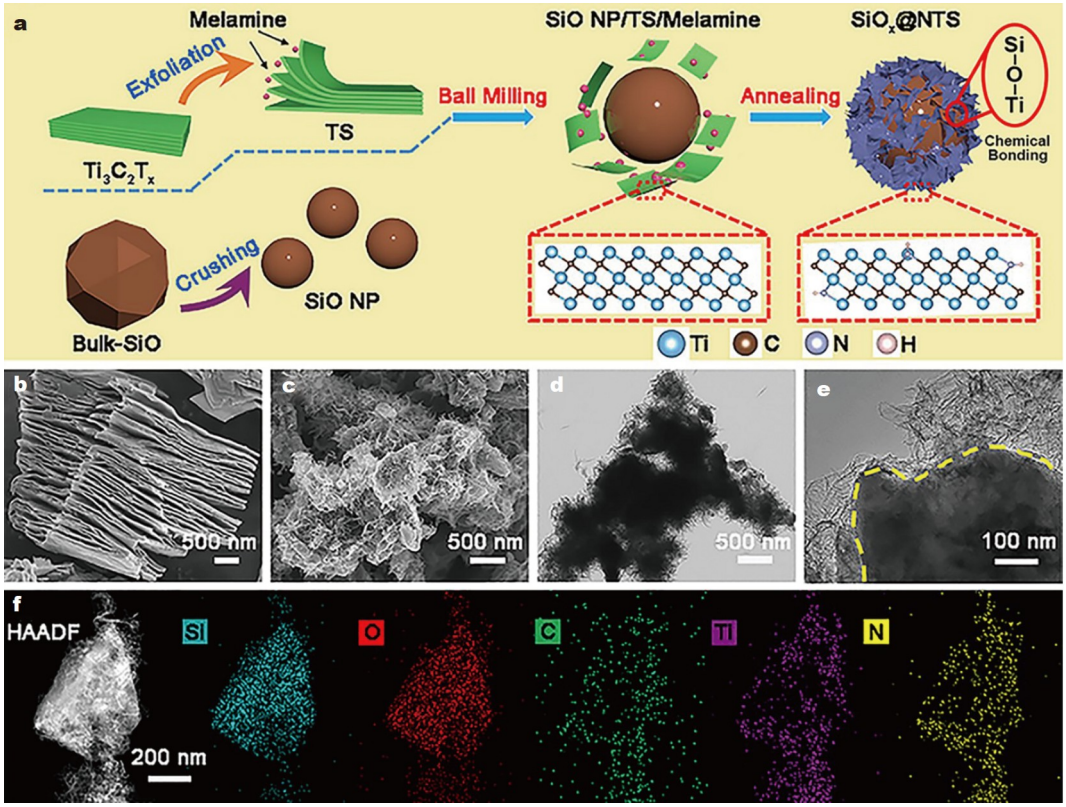

Figure 1 (a) Schematic of the synthetic route for the SiO_x@NTS; SEM images of (b) multilayered $Ti_3C_2T_x$ MXene and (c) SiO_x@NTS; (d) TEM and (e) HRTEM images of the SiO_x@NTS. (f) HAADF-STEM images and the elemental maps of the SiO_x@NTS.

atomic numbers for SiO_x and NTS also verified the core-shell structure of the SiO_x@NTS. For comparison, the SiO_x/T prepared without the assistance of melamine was composed of block $Ti_3C_2T_x$ MXene and SiO_x NPs, without any special architecture (Figs S5 and S6).

The components and structure of the SiO_x@NTS were further explored by XRD, Raman spectroscopy, and N_2 adsorption/desorption measurements. In the XRD pattern (Fig. 2a), four sharp peaks (6°, 36°, 42°, and 61°) agreed well with the previously reported few-layered $Ti_3C_2T_x$ MXene derived from the NH_4^+ intercalation method [36]. In the Raman spectrum (Fig. 2b), the peak at 500 cm^{-1} was the characteristic peak of SiO_x [37], and the two peaks at 1340 and 1600 cm^{-1} corresponded to the D and G bands of layered materials, respectively [38]. The XRD and Raman results confirmed that the SiO_x@NTS composite was composed of SiO_x and $Ti_3C_2T_x$. The N_2 adsorption/desorption measurements were determined to reveal the surface areas of the SiO_x@NTS and SiO_x@T. As shown in Fig. 2c, the calculated BET surface area of the SiO_x@NTS was 106.9 $m^2\ g^{-1}$, which was considerably larger than that of the SiO_x@T (28.8 $m^2\ g^{-1}$) (Fig. S7). Such stark contrast demonstrated the efficient exfoliation of $Ti_3C_2T_x$ MXene by melamine-assisted ball milling. FTIR and XPS were used to investigate the composition and electronic structure of the SiO_x@NTS, respectively. Fig. 2d exhibits the FTIR spectrum of the SiO_x@NTS, where the peaks at 3405 and 1656 cm^{-1} were attributed to the stretching vibration of O–H and C=O bonds [39], respectively, and derived from the abundant oxygen-containing groups on the NTS. The peaks at 1510 and 1410 cm^{-1} were correlated with the vibration of the N–Ti bond [40,41]. A weak peak at 661 cm^{-1} represented the Ti–O–Ti bond from the NTS. Three peaks at 1086, 798, and 472 cm^{-1} were attributed to the asymmetric stretching vibration and bending vibration of the Si–O–Si bond in SiO_x [42]. Moreover, a signal of the Si–O–Ti bond can be detected at around 950 cm^{-1}, confirming the bonding linkage between SiO_x NPs and the NTS [43]. Fig. 2e shows the XPS survey spectra of the SiO_x@NTS and SiO_x@T, revealing the presence of Si, O, C, and Ti in the two samples. The SiO_x@NTS also showed a peak at 398 eV, which corresponded to N 1s. In the O 1s spectrum of the SiO_x@NTS (Fig. 2f), four fitting peaks at 533.2, 532.6, 532.1, and 531.2 eV accorded with the Ti–OH, Si–O–Si, Si–O–Ti, and Ti–O bonds, respectively [32]. The high intensity of the Si–O–Ti bond verified the strong interaction between SiO_x and the NTS, which can accelerate the interfacial electron transport and strengthen the structural stability of the SiO_x@NTS. As for the Si 2p spectrum (Fig. 2g), five peaks were observed at 103.8, 103.2, 102.6, 101.9, and 99.6 eV, corresponding to Si^{4+}, Si^{3+}, Si^{2+}, Si^{1+}, and Si^0, respectively [44]. The C 1s spectrum (Fig. S8) showed four peaks at 288.4, 285.8, 284.8, and 284.3 eV, which were related to C–O, C–N, C–C, and C–Ti bonds, respectively [45]. Fig. 2h shows the Ti 2p spectrum; the observed Ti–O, Ti–N, and Ti–C bindings in Fig. 2h agreed well with those in previous literature [46,47]. The N 1s spectrum indicated the successful incorporation of N, including pyrrolic N (400.3 eV), pyridinic N (398.3 eV), and Ti–N (396.5 eV), in the composite (Fig. 2i) [48]. The above FTIR and XPS results confirm the presence of Ti–N and C–N bonds in the composite, revealing the successful nitrogen doping in the NTS.

To understand the roles of melamine in $Ti_3C_2T_x$ MXene exfoliation, we first removed SiO from the recipe and conducted

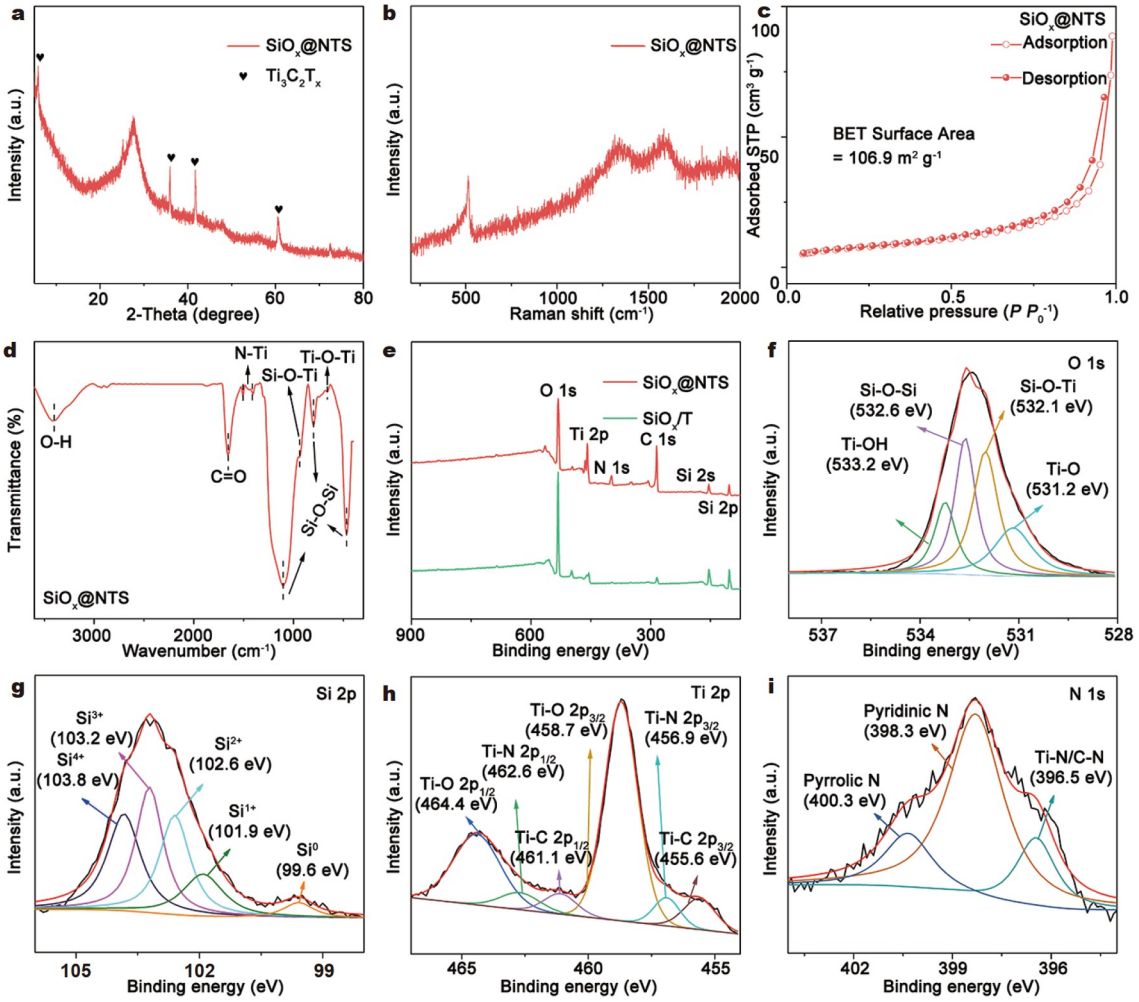

Figure 2 (a) XRD pattern, (b) Raman spectrum, (c) N_2 sorption isotherm, and (d) FTIR spectrum of the SiO_x@NTS. (e) XPS survey spectra of the SiO_x@NTS and SiO_x/T. (f) O 1s, (g) Si 2p, (h) Ti 2p, and (i) N 1s spectra of the SiO_x@NTS.

AFM measurements to reveal the effects of different molecules (melamine, triazine, 1,3,5-triaminobenzene, and 2,4,6-trimethyl-1,3,5-triazine) on the exfoliation process. As shown in Fig. 3a, several small sheets with a thickness of ~4 nm can be observed, revealing the sufficient exfoliation achieved by melamine. Then, to determine the priority of N species in melamine (triazine ring or $-NH_2$) for the exfoliation process, we replaced melamine with triazine and 2,4,6-trimethyl-1,3,5-triazine. The results are exhibited in Fig. 3b, d, in which the thicknesses of the products were ~80 or ~110 nm, respectively, indicating a noneffective exfoliation process with triazine or 2,4,6-trimethyl-1,3,5-triazine. As for 1,3,5-triaminobenzene, the triazine ring in melamine was replaced with a benzene ring, and the product in Fig. 3c implied a height of ~60 nm. Different additive-derived AFM results indicated that the structural characteristics of melamine ($-NH_2$ attached triazine ring) were the key to the successful exfoliation. For a deep understanding of this result, the models of different additive molecules adsorbed on the Ti_3C_2 sheet were constructed by DFT calculations. The charge accumulation (yellow)/depletion (cyan) between additives and the Ti_3C_2 sheet and their geometric structures were calculated, and the results are summarized in Fig. 3a–d. The adsorption energies of melamine (E_a = −5.522 eV), triazine (E_b = −2.872 eV), 1,3,5-triaminobenzene (E_c = −4.379 eV), and 2,4,6-trimethyl-1,3,5-triazine (E_d = −0.927 eV) on the Ti_3C_2 sheet agreed well with the AFM results (Fig. 3e). The lowest adsorption energy of melamine revealed its best adsorption stability on the Ti_3C_2 sheet derived from unique amino and triazine groups. During the ball-milling process, this strong binding benefited the intercalation of melamine into the space of the TS and the exfoliation with the impact of the ball. To reveal the effect of SiO on exfoliation, we also obtained the AFM image of the HF-etched SiO_x@NTS (Fig. S9). The thickness of the NTS in the SiO_x@NTS was similar to that of the product in Fig. 3a, but the morphology was different, indicating that the SiO component in the recipe can only change the morphology of MXene but not the thickness.

The lithium storage properties of the SiO_x@NTS and SiO_x/T were measured to study the influence of NTS on the performance. As shown in the CV curves of the SiO_x@NTS (Fig. 4a), a broad peak appeared at around 1.1 V in the first cycle and disappeared in the following cycles, resulting from the irreversible reactions between the electrolyte and terminal groups of the NTS [49]. For the second and third cycles, the anodic peak at ~0.57 V represented the de-alloying process of SiO_x [50]. Fig. 4b shows the charge/discharge voltage profiles of the SiO_x@NTS and SiO_x/T at 0.1 A g^{-1}. The first discharge/charge capacities of

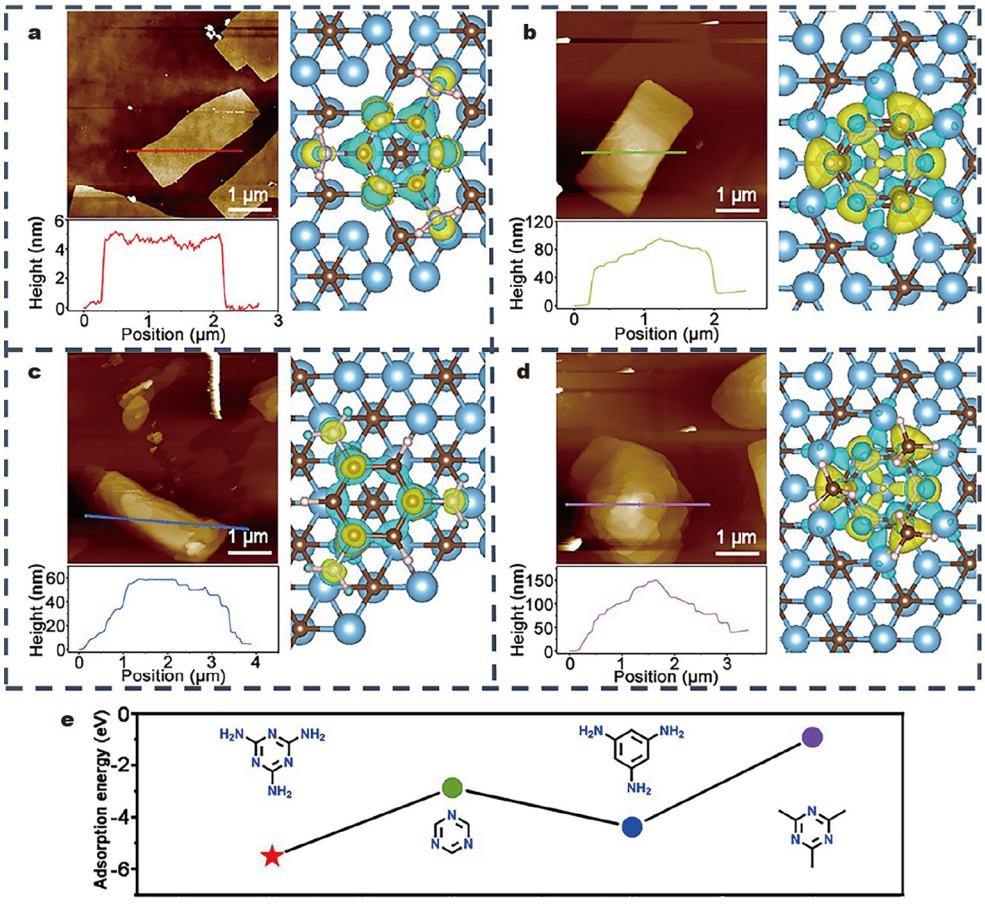

Figure 3 AFM images, height profiles of $Ti_3C_2T_x$ MXene exfoliated by different additives, and charge density differences at the interface between the additives and the TS: (a) melamine, (b) triazine, (c) 1,3,5-triaminobenzene, and (d) 2,4,6-trimethyl-1,3,5-triazine. (e) Adsorption energies of different additives on $Ti_3C_2T_x$ MXene.

SiO_x@NTS were 1882.1/1014.1 mA h g^{-1}, delivering a higher initial Coulombic efficiency (CE) of 54%, in contrast to the value of 46% for SiO_x/T. Fig. 4c exhibits the cycling performance of the SiO_x@NTS and SiO_x/T at 0.5 A g^{-1}. The SiO_x@NTS maintained a high capacity of 1141.3 mA h g^{-1} after 100 cycles, which was notably superior to the value of 335.7 mA h g^{-1} for the SiO_x/T. The NTS cycles were steady, but the NTS capacity was low, indicating that the capacity of the SiO_x@NTS was mainly contributed by the SiO_x component. The composites of SiO_x and MXene were prepared using triazine, 1,3,5-triaminobenzene, and 2,4,6-trimethyl-1,3,5-triazine (molecule formula in Fig. 3) as additives. Then, their cycling performances were measured. As shown in Fig. S10, the capacities of all the composites gradually decayed upon cycling. After 500 cycles at 1.0 A g^{-1}, the specific capacities were less than ~300 mA h g^{-1}. Meanwhile, the composite using melamine as the additive had a capacity of ~800 mA h g^{-1}, which was substantially higher than those of other composites. The comparison demonstrated the advantages of melamine as an additive. The SiO_x@NTS also exhibited a notably better rate capability than the SiO_x/T (Fig. 4d). Discharge capacities of 1302.7, 1179.7, 1068.1, 811.9, 708.9, and 596.4 mA h g^{-1} were obtained for the SiO_x@NTS at the current densities of 0.1, 0.5, 1.0, 2.0, 3.0, and 5.0 A g^{-1}, respectively. As the current density returned to 0.5 A g^{-1}, the SiO_x@NTS attained a high capacity of 1103.2 mA h g^{-1}. The long-term cycling performance of the SiO_x@NTS was also measured at 1.0 A g^{-1}. As shown in Fig. 4e, the SiO_x@NTS retained a capacity of ~700 mA h g^{-1} over 800 cycles with nearly 100% CE at a mass loading of ~1.2 mg cm^{-2}. Fig. S11 shows the charge/discharge voltage profiles for more cycles. Although the capacity slowly decayed with the cycles, the profile contour was retained, indicating the same electrochemical reactions in the cycles. As the mass loading of active material is a key point for its possible commercial application, the areal capacity of the SiO_x@NTS under different mass loadings was tested (Fig. 4f). The SiO_x@NTS electrodes were first activated at 0.2 mA cm^{-2} for three cycles and then cycled at 1.0 mA cm^{-2} for 100 cycles. The areal capacity of the SiO_x@NTS reached 0.82, 1.34, 1.79, and 2.11 mA h cm^{-2} (50th cycle) at the mass loadings of 0.78, 1.22, 1.54, and 1.98 mg cm^{-2}, respectively. Furthermore, the areal capacity of the SiO_x@NTS at 0.2 mA cm^{-2} increased almost linearly with the mass loading range from 0.78 to 1.98 mg cm^{-2} (Fig. 4g). At an ultrahigh loading of 3.5 mg cm^{-2} (Fig. 4h), the SiO_x@NTS delivered a high areal capacity (2.5 mA h cm^{-2}, 2nd cycle under 0.2 mA cm^{-2}) and good cycling stability (1.58 mA h cm^{-2}, 300th cycle under 1.0 mA cm^{-2}). The cycling performance of the SiO_x@NTS was examined at a high mass loading of 4.5 mg cm^{-2}. As displayed in Fig. S12, the areal capacity of the SiO_x@NTS decayed rapidly from ~4 to ~1 mA h cm^{-2}. This result may be related to the inferior reaction kinetics and structural stability caused by the thick electrode. The superior Li storage properties of the SiO_x@NTS composite

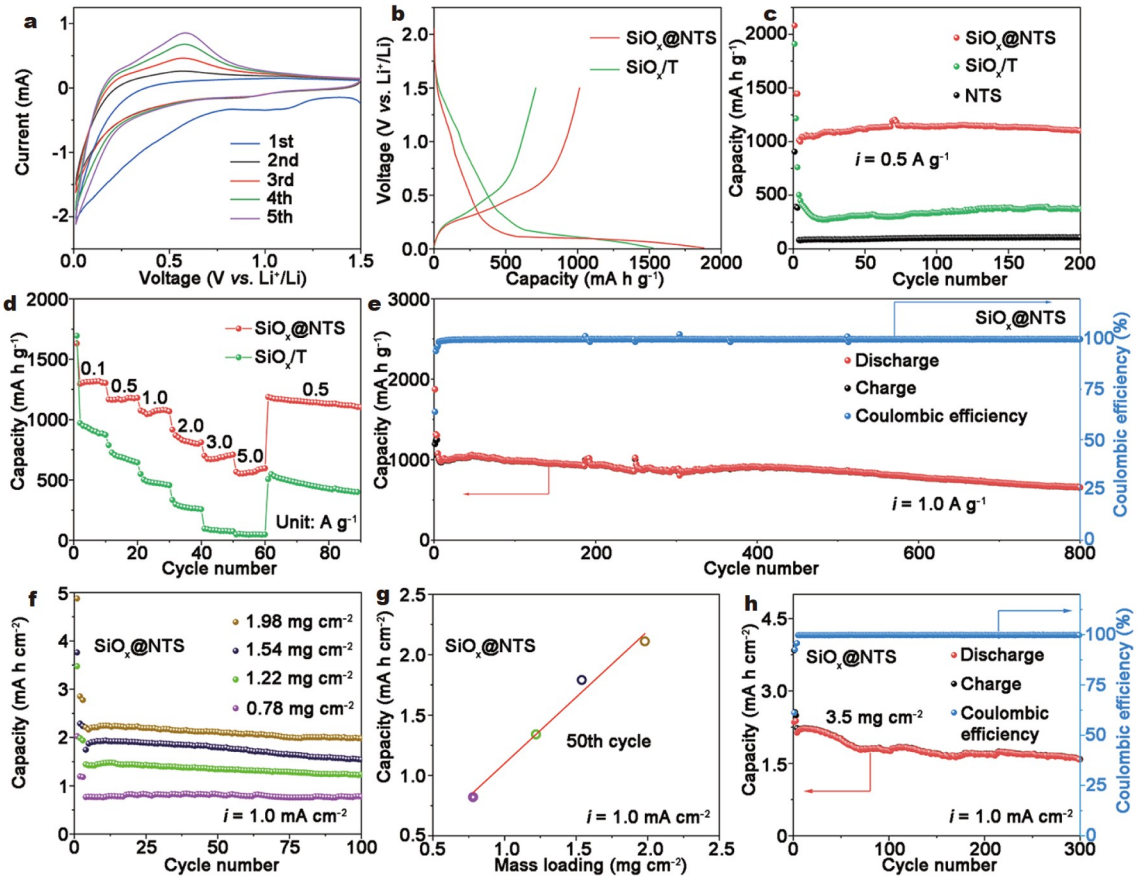

Figure 4 (a) CV curves of the SiO_x@NTS at 0.1 mV s^{-1}. (b) Charge and discharge voltage profiles of the SiO_x@NTS and SiO_x/T. (c) Cycling performances of the SiO_x@NTS and SiO_x/T at 0.5 A g^{-1}. (d) Rate capabilities of the SiO_x@NTS and SiO_x/T. (e) Long-term cycling performance of SiO_x@NTS at 1.0 A g^{-1}. (f) Cycling performance of SiO_x@NTS in the mass loading range from 0.78 to 1.98 mg cm^{-2}, and (g) the corresponding area capacity at 1.0 mA cm^{-2}. (h) Cycling performance of the SiO_x@NTS at a high mass loading of 3.5 mg cm^{-2} under 1.0 mA cm^{-2}.

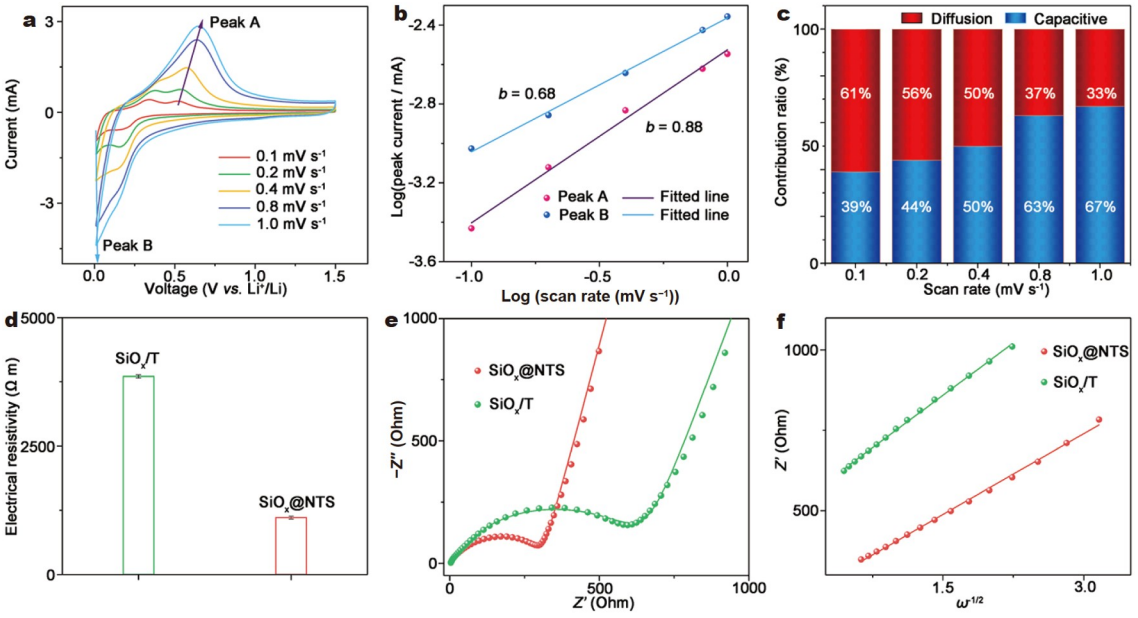

Figure 5 (a) CV curves of the SiO_x@NTS at different scan rates. (b) Fitted lines and the calculated *b*-values derived from log(*i*) *vs.* log(*v*). (c) Contribution ratios of diffusion and capacitive charge storage at different scan rates. (d) Electrical resistivities of the SiO_x@NTS and SiO_x/T. (e) Nyquist plots and (f) the relationships between Z' and $\omega^{-1/2}$ for the SiO_x@NTS and SiO_x/T electrodes.

demonstrated its great application prospect.

The CV curves of the SiO_x@NTS at the scan rates of 0.1–1.0 mV s^{-1} were measured to clarify the pseudocapacitance contribution (Fig. 5a). By measuring the current (i) of peak A and peak B and combining Equation (1) [51] below, the capacitance characteristic of the SiO_x@NTS was studied:

$$i = av^b, \quad (1)$$

$$i = k_1v + k_2v^{1/2}. \quad (2)$$

The b-value was calculated to distinguish the lithium diffusion-controlled (b = 0.5) or pseudocapacitive-controlled (b = 1.0) behaviors. The plots of log(i) *vs.* log(v) provided the b-values of peaks A and B at 0.88 and 0.68 in Fig. 5b, respectively, indicating that both behaviors contributed to lithium storage in the SiO_x@NTS [52]. Similar results have been well documented in the literature [53]. The combination of two behaviors enabled the composite to process the high capacity of SiO_x and the fast kinetics of the NTS, thereby showing a good electrochemical performance. The capacitive contribution ratio was calculated by Equation (2), in which k_1v and $k_2v^{1/2}$ represent the contributions of capacity and diffusion, respectively. As shown in Fig. 5c, the capacitive contribution accounted for a high percentage with the increase in the scan rate, which is beneficial to fast charge/discharge and good cycling stability. A high capacitive contribution of 50% was delivered at the scan rate of 0.4 mV s^{-1} (Fig. S13). Fig. 5d shows the electrical resistivity comparison of the SiO_x@NTS and SiO_x/T. The SiO_x@NTS had a significantly reduced electrical resistivity, in contrast to that of the SiO_x/T (1103 *vs.* 3848 Ω m), indicating an enhanced electron transfer rate for the SiO_x@NTS. The enhanced reaction kinetics of the SiO_x@NTS over SiO_x/T was revealed by EIS measurements (Fig. 5e). The equivalent circuit and the detailed EIS parameters of the SiO_x@NTS and SiO_x/T electrodes are shown in Fig. S14 and Table S1, respectively. The SiO_x@NTS exhibited a smaller charge-transfer impedance (R_{ct}) resistance than the SiO_x/T (176 *vs.* 307 Ω), demonstrating a faster charge-transfer kinetics. The Li-ion diffusion coefficient (D_{Li^+}) can be quantitatively calculated using Equation (3) [54]:

$$D_{Li^+} = 0.5\left(\frac{RT}{AF^2\sigma C}\right)^2, \quad (3)$$

where R, T, A, F, C, and σ are the gas constant, absolute temperature, the surface area of the electrode, the number of electrons per molecule during oxidization, Faraday constant, Li-ion concentration, and the Warburg factor, respectively. The σ-value is related to the slope of Z' *versus* $\omega^{-1/2}$ in the low-frequency region according to Equation (4):

$$Z' = R_D + R_L + \sigma\omega^{-1/2}. \quad (4)$$

By calculations, the SiO_x@NTS showed a smaller slope of Z' *versus* $\omega^{-1/2}$ than the SiO_x/T, which indicated its faster Li-ion diffusion rate. The Warburg factor (σ) and Li-ion diffusion coefficient (D_{Li^+}) are provided in Supplementary information (Table S2). Compared with SiO_x/T, the SiO_x@NTS had a smaller Warburg factor (σ) and a larger Li-ion diffusion coefficient (D_{Li^+}), confirming the enhanced charge-transfer kinetics. Based on the above results, the charge transfer and ion diffusion kinetics of the SiO_x@NTS were greatly enhanced by the introduction of the NTS.

Fig. 6a, b schematically illustrate the volume changes in the

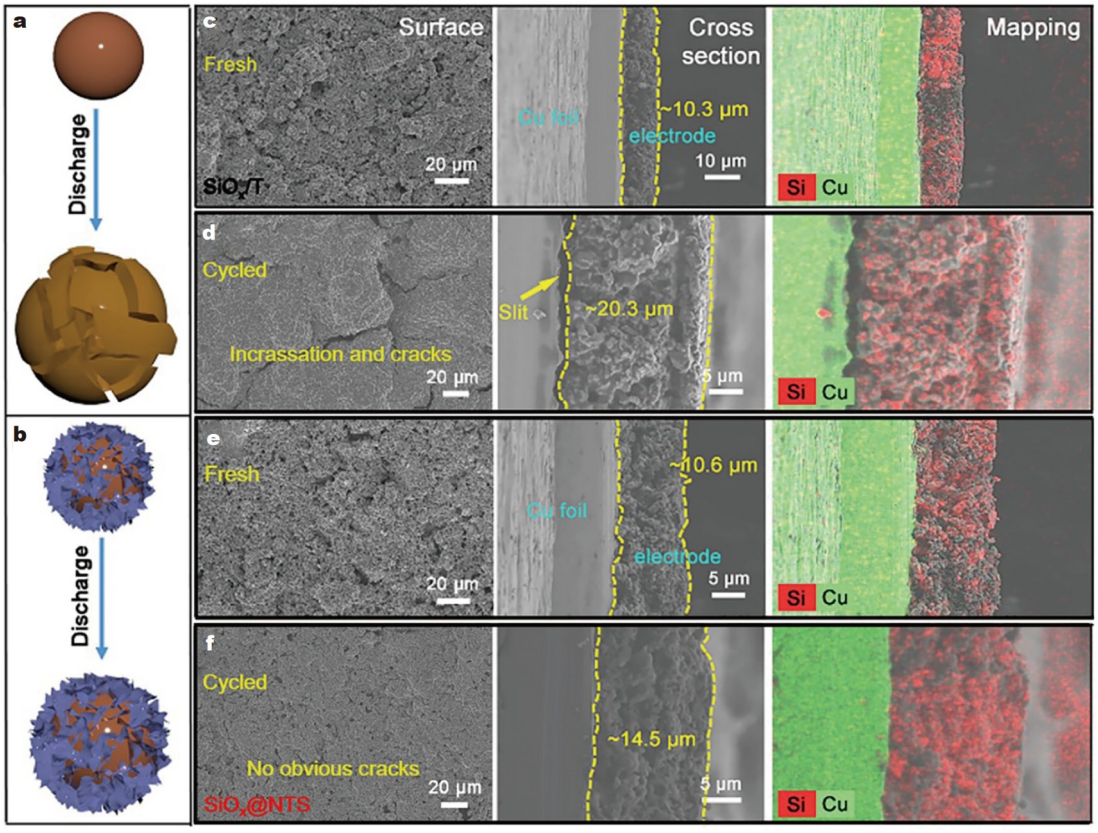

Figure 6 Schematic of (a) the SiO_x/T and (b) SiO_x@NTS electrodes during the discharging process. SEM and the corresponding EDS mapping images of (c and d) SiO_x/T and (e and f) SiO_x@NTS electrodes.

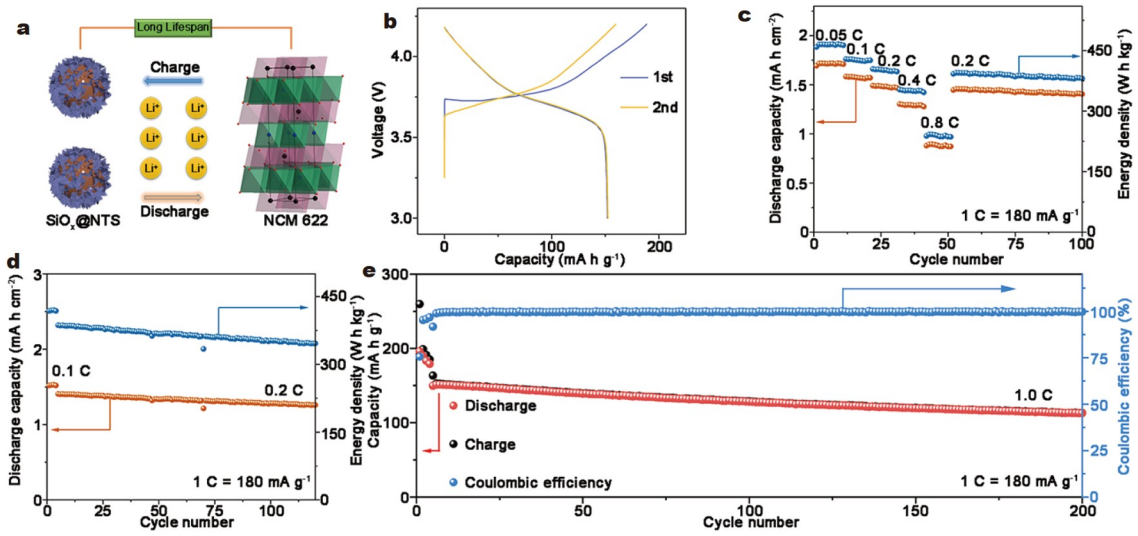

Figure 7 (a) Schematic of the SiO_x@NTS//NCM622 full cell. (b) Charge and discharge voltage profiles. (c) Rate capability and the corresponding energy density of the SiO_x@NTS//NCM622 full cells. (d) Cycling performance and the corresponding energy density of the SiO_x@NTS//NCM622 full cells. (e) Long-term cycling performance of the SiO_x@NTS//NCM622 full cell at 1.0 C.

SiO_x/T and SiO_x@NTS, respectively. The SiO_x particles in the SiO_x/T composite were fractured during charging, whereas the volume expansion of SiO_x particles in the core-shell SiO_x@NTS was restricted by the NTS shell. To prove this phenomenon, we characterized the SiO_x/T and SiO_x@NTS electrodes before and after cycling by SEM and EDS mapping (Fig. 6c–f). Before cycling, both the surfaces of the two electrodes were porous and full of irregular particles (Fig. 6c, e). After charging and discharging at 0.5 A g^{-1} 200 times, the SiO_x/T electrode became incrassated by 97.1%, and several cracks appeared (Fig. 6d). On the contrary, the SiO_x@NTS electrode showed no evident cracks after 200 cycles, and the thickness enlarged by 36.8%. Furthermore, a distinct slit appeared on the interface of the Cu foil and SiO_x/T. In comparison, the SiO_x@NTS was still tightly bounded with the current collector. These results reveal the advantages of the NTS in restricting volume changes and strongly interacting with the current collector.

To evaluate the application prospect of the SiO_x@NTS anode, we employed a $LiNi_{0.6}Co_{0.2}Mn_{0.2}O_2$ (NCM622) cathode to assemble SiO_x@NTS//NCM622 full cells (Fig. 7a). Fig. S15 presents the performance of NCM622. The capacity ratio of the cathode to the anode was controlled at 1.1:1. Fig. 7b shows the charging/discharging voltage profiles of the Li-ion full cell at 0.1 C (1 C = 180 mA g^{-1}) between 3.0 and 4.2 V. Fig. 7c depicts the rate capability of the Li-ion full cell at a cathode mass loading of ~10 mg cm^{-2}. High areal capacities of 1.73 and 1.57 mA h cm^{-2} were delivered at 0.05 and 0.1 C, respectively. When the current density increased to 0.2, 0.4, and 0.8 C, the Li-ion full cell retained areal capacities of 1.48, 1.31, and 0.88 mA h cm^{-2}, respectively. After the current density returned to 0.2 C, the original capacity was recovered, suggesting a remarkable rate capability of the Li-ion full cell. Fig. 7d show the cycling performances of the Li-ion full cell at a high cathode mass loading of ~10.0 mg cm^{-2}, which was calculated using areal and mass capacities. At a current density of 0.2 C, the full cell delivered a high areal capacity of 1.28 mA h cm^{-2} over 100 cycles, corresponding to a capacity retention of 90% (Fig. 7d). At a high current density of 1 C, it retained 113 mA h g^{-1} capacity over 200 cycles (Fig. 7e). Meanwhile, the corresponding energy densities were also calculated by averaging the discharge voltage during cycling, and the results are summarized in Fig. 7c, d. The full cell achieved high-energy densities of 459 W h kg^{-1} at 0.05 C and 381 W h kg^{-1} at 0.2 C after 100 cycles. The excellent electrochemical performance of the Li-ion full cell reveals the highly promising prospect of the SiO_x@NTS anodes for LIBs.

CONCLUSIONS

In summary, we developed a unique and facile strategy to construct the SiO_x@NTS and investigated its electrochemical performance for LIBs. The NTS can reinforce the reaction kinetics and buffer the volume expansion of SiO_x by forming Si–O–Ti bond and coating on the surface of SiO_x. The SiO_x@NTS anode showed a high capacity of ~700 mA h g^{-1} over 800 cycles at 1.0 A g^{-1}. It also delivered a good cycling performance at high mass loadings and maintained an areal capacity of 1.58 mA h cm^{-2} after 300 cycles at 1.0 mA cm^{-2}. The SiO_x@NTS//NCM622 full cell also retained a high areal capacity of 1.28 mA h cm^{-2} over 100 cycles, indicating an exciting application prospect.

Received 3 April 2022; accepted 30 May 2022; published online 23 August 2022

1 Xue H, Wu Y, Zou Y, *et al.* Unraveling metal oxide role in exfoliating graphite: New strategy to construct high-performance graphene-modified SiO_x-based anode for lithium-ion batteries. Adv Funct Mater, 2020, 30: 1910657
2 Zhou X, Liu Y, Ren Y, *et al.* Engineering molecular polymerization for template-free SiO_x/C hollow spheres as ultrastable anodes in lithium-ion batteries. Adv Funct Mater, 2021, 31: 2101145
3 Tian H, Tian H, Yang W, *et al.* Stable hollow-structured silicon suboxide-based anodes toward high-performance lithium-ion batteries. Adv Funct Mater, 2021, 31: 2101796
4 Park CM, Choi W, Hwa Y, *et al.* Characterizations and electrochemical behaviors of disproportionated SiO and its composite for rechargeable Li-ion batteries. J Mater Chem, 2010, 20: 4854–4860
5 Yoo H, Park E, Kim H, *et al.* A swelling-suppressed Si/SiO_x nanosphere lithium storage material fabricated by graphene envelopment. Chem

Commun, 2016, 52: 8030–8033
6 Liu Z, Zhao Y, He R, *et al.* Yolk@shell SiO/C microspheres with semi-graphitic carbon coating on the exterior and interior surfaces for durable lithium storage. Energy Storage Mater, 2019, 19: 299–305
7 Lee SJ, Kim HJ, Hwang TH, *et al.* Delicate structural control of Si-SiO_x-C composite *via* high-speed spray pyrolysis for Li-ion battery anodes. Nano Lett, 2017, 17: 1870–1876
8 Fu R, Ji J, Yun L, *et al.* Graphene wrapped silicon suboxides anodes with suppressed Li-uptake behavior enabled superior cycling stability. Energy Storage Mater, 2021, 35: 317–326
9 Li G, Li JY, Yue FS, *et al.* Reducing the volume deformation of high capacity SiO_x/G/C anode toward industrial application in high energy density lithium-ion batteries. Nano Energy, 2019, 60: 485–492
10 Xu Q, Sun JK, Yin YX, *et al.* Facile synthesis of blocky SiO_x/C with graphite-like structure for high-performance lithium-ion battery anodes. Adv Funct Mater, 2018, 28: 1705235
11 Yang M, Jin L, He M, *et al.* SiO_x@C composites obtained by facile synthesis as anodes for lithium- and potassium-ion batteries with excellent electrochemical performance. Appl Surf Sci, 2021, 542: 148712
12 Raza A, Jung JY, Lee CH, *et al.* Swelling-controlled double-layered SiO_x/Mg_2SiO_4/SiO_x composite with enhanced initial Coulombic efficiency for lithium-ion battery. ACS Appl Mater Interfaces, 2021, 13: 7161–7170
13 Gong Q, Wang H, Song W, *et al.* Tunable synthesis of hierarchical yolk/double-shelled SiO_x@TiO_2@C nanospheres for high-performance lithium-ion batteries. Chem Eur J, 2021, 27: 2654–2661
14 Wang L, Zhang B, Hu Y, *et al.* Failure analysis of $LiNi_{0.83}Co_{0.12}Mn_{0.05}O_2$/graphite-$SiO_x$ pouch batteries cycled at high temperature. J Power Sources, 2021, 482: 228978
15 Wu S, Yang Y, Liu C, *et al. In-situ* polymerized binder: A three-in-one design strategy for all-integrated SiO_x anode with high mass loading in lithium ion batteries. ACS Energy Lett, 2021, 6: 290–297
16 Liu D, Jiang Z, Zhang W, *et al.* Micron-sized SiO_x/N-doped carbon composite spheres fabricated with biomass chitosan for high-performance lithium-ion battery anodes. RSC Adv, 2020, 10: 38524–38531
17 Wang L, Zhu X, Tu K, *et al.* Synthesis of carbon-SiO_2 hybrid layer@-SiO_2@CNT coaxial nanotube and its application in lithium storage. Electrochim Acta, 2020, 354: 136726
18 Xu Q, Sun JK, Yu ZL, *et al.* SiO_x encapsulated in graphene bubble film: An ultrastable Li-ion battery anode. Adv Mater, 2018, 30: 1707430
19 Zhang K, Du W, Qian Z, *et al.* SiO_x embedded in N-doped carbon nanoslices: A scalable synthesis of high-performance anode material for lithium-ion batteries. Carbon, 2021, 178: 202–210
20 Xia M, Chen B, Gu F, *et al.* $Ti_3C_2T_x$ MXene nanosheets as a robust and conductive tight on Si anodes significantly enhance electrochemical lithium storage performance. ACS Nano, 2020, 14: 5111–5120
21 Naguib M, Kurtoglu M, Presser V, *et al.* Two-dimensional nanocrystals produced by exfoliation of Ti_3AlC_2. Adv Mater, 2011, 23: 4248–4253
22 Zeng Z, Fu G, Yang HB, *et al.* Bifunctional N-$CoSe_2$/3D-MXene as highly efficient and durable cathode for rechargeable Zn-air battery. ACS Mater Lett, 2019, 1: 432–439
23 Xiao Z, Li Z, Meng X, *et al.* MXene-engineered lithium-sulfur batteries. J Mater Chem A, 2019, 7: 22730–22743
24 Anasori B, Lukatskaya MR, Gogotsi Y. 2D metal carbides and nitrides (MXenes) for energy storage. Nat Rev Mater, 2017, 2: 16098
25 Han P, Liu F, Zhang Y, *et al.* Organic-inorganic hybridization engineering of polyperylenediimide cathodes for efficient potassium storage. Angew Chem Int Ed, 2021, 60: 23596–23601
26 Luo Z, Liu L, Ning J, *et al.* A microporous covalent-organic framework with abundant accessible carbonyl groups for lithium-ion batteries. Angew Chem Int Ed, 2018, 57: 9443–9446
27 Zhang X, Li J, Li J, *et al.* 3D TiO_2@nitrogen-doped carbon/Fe_7S_8 composite derived from polypyrrole-encapsulated alkalized MXene as anode material for high-performance lithium-ion batteries. Chem Eng J, 2020, 385: 123394
28 Li J, Han L, Li Y, *et al.* MXene-decorated SnS_2/Sn_3S_4 hybrid as anode material for high-rate lithium-ion batteries. Chem Eng J, 2020, 380: 122590
29 Zhu Z, Ni Y, Lv Q, *et al.* Surface plasmon mediates the visible light-responsive lithium-oxygen battery with Au nanoparticles on defective carbon nitride. Proc Natl Acad Sci USA, 2021, 118: e2024619118
30 Zhang CJ, McKeon L, Kremer MP, *et al.* Additive-free MXene inks and direct printing of micro-supercapacitors. Nat Commun, 2019, 10: 1795
31 Li X, Chen Z, Li A, *et al.* Three-dimensional hierarchical porous structures constructed by two-stage MXene-wrapped Si nanoparticles for Li-ion batteries. ACS Appl Mater Interfaces, 2020, 12: 48718–48728
32 Hui X, Zhao R, Zhang P, *et al.* Low-temperature reduction strategy synthesized Si/Ti_3C_2 MXene composite anodes for high-performance Li-ion batteries. Adv Energy Mater, 2019, 9: 1901065
33 Sun X, Wang Y, Zhang Y, *et al.* Efficient lithium storage of Si-based anode enabled by a dual-component protection strategy. Adv Energy Sustain Res, 2022, 3: 2200028
34 Song Y, Sun Z, Fan Z, *et al.* Rational design of porous nitrogen-doped Ti_3C_2 MXene as a multifunctional electrocatalyst for Li-S chemistry. Nano Energy, 2020, 70: 104555
35 Zuo D, Song S, An C, *et al.* Synthesis of sandwich-like structured Sn/SnO_x@MXene composite through *in-situ* growth for highly reversible lithium storage. Nano Energy, 2019, 62: 401–409
36 Zhang S, Huang P, Wang J, *et al.* Fast and universal solution-phase flocculation strategy for scalable synthesis of various few-layered MXene powders. J Phys Chem Lett, 2020, 11: 1247–1254
37 Hu G, Zhong K, Yu R, *et al.* Enveloping SiO_x in N-doped carbon for durable lithium storage *via* an eco-friendly solvent-free approach. J Mater Chem A, 2020, 8: 13285–13291
38 Zhao R, Qian Z, Liu Z, *et al.* Molecular-level heterostructures assembled from layered black phosphorene and Ti_3C_2 MXene as superior anodes for high-performance sodium ion batteries. Nano Energy, 2019, 65: 104037
39 Zhao R, Wang M, Zhao D, *et al.* Molecular-level heterostructures assembled from titanium carbide MXene and Ni-Co-Al layered double-hydroxide nanosheets for all-solid-state flexible asymmetric high-energy supercapacitors. ACS Energy Lett, 2018, 3: 132–140
40 Kong B, Tang J, Zhang Y, *et al.* Incorporation of well-dispersed sub-5-nm graphitic pencil nanodots into ordered mesoporous frameworks. Nat Chem, 2016, 8: 171–178
41 Cui Z, Zu C, Zhou W, *et al.* Mesoporous titanium nitride-enabled highly stable lithium-sulfur batteries. Adv Mater, 2016, 28: 6926–6931
42 Sohn M, Park HI, Kim H. Foamed silicon particles as a high capacity anode material for lithium-ion batteries. Chem Commun, 2017, 53: 11897–11900
43 Ren J, Li Z, Liu S, *et al.* Silica-titania mixed oxides: Si-O-Ti connectivity, coordination of titanium, and surface acidic properties. Catal Lett, 2008, 124: 185–194
44 Zhang Y, Mu Z, Lai J, *et al.* MXene/Si@SiO_x@C layer-by-layer superstructure with autoadjustable function for superior stable lithium storage. ACS Nano, 2019, 13: acsnano.8b08821
45 Bao W, Liu L, Wang C, *et al.* Facile synthesis of crumpled nitrogen-doped MXene nanosheets as a new sulfur host for lithium-sulfur batteries. Adv Energy Mater, 2018, 8: 1702485
46 He F, Tang C, Zhu G, *et al.* Leaf-inspired design of mesoporous Sb_2S_3/N-doped $Ti_3C_2T_x$ composite towards fast sodium storage. Sci China Chem, 2021, 64: 964–973
47 Zhang S, Ying H, Guo R, *et al.* Vapor deposition red phosphorus to prepare nitrogen-doped $Ti_3C_2T_x$ MXenes composites for lithium-ion batteries. J Phys Chem Lett, 2019, 10: 6446–6454
48 Pang Q, Tang J, Huang H, *et al.* A nitrogen and sulfur dual-doped carbon derived from polyrhodanine@cellulose for advanced lithium-sulfur batteries. Adv Mater, 2015, 27: 6021–6028
49 Liu YT, Zhang P, Sun N, *et al.* Self-assembly of transition metal oxide nanostructures on MXene nanosheets for fast and stable lithium storage. Adv Mater, 2018, 30: 1707334
50 Zhang K, Mao H, Gu X, *et al.* ZIF-derived cobalt-containing N-doped carbon-coated SiO_x nanoparticles for superior lithium storage. ACS Appl Mater Interfaces, 2020, 12: 7206–7211
51 Wu Y, Nie P, Wu L, *et al.* 2D MXene/SnS_2 composites as high-performance anodes for sodium ion batteries. Chem Eng J, 2018, 334: 932–938
52 Xu X, Chen B, Hu J, *et al.* Heterostructured TiO_2 spheres with tunable

interiors and shells toward improved packing density and pseudocapacitive sodium storage. Adv Mater, 2019, 31: 1904589
53 Meng R, Huang J, Feng Y, *et al.* Black phosphorus quantum dot/Ti_3C_2 MXene nanosheet composites for efficient electrochemical lithium/sodium-ion storage. Adv Energy Mater, 2018, 8: 1801514
54 Li Z, Zhao H, Lv P, *et al.* Watermelon-like structured SiO_x-TiO_2@C nanocomposite as a high-performance lithium-ion battery anode. Adv Funct Mater, 2018, 28: 1605711

Acknowledgements This work was supported by the National Natural Science Foundation of China (21971146 and 52171182), Taishan Scholarship in Shandong Province (ts201511004), the Key Research and Development Program of Shandong Province (2021ZLGX01), and the HPC Cloud Platform of Shandong University. The authors thank the equipment support from Shandong University Structural Constituent and Physical Property Research Facilities for the high-energy ball-milling machine (Fritsch Pulverisette 7, Germany) and AFM (Bruker Bioscope Resolve, Germany).

Author contributions Zhang K conceived the idea, performed the experiments and data analysis, and wrote the original draft. Zhao D performed the calculation. Qian Z guided the calculation process. Gu X, Yang J, and Qian Y guided the idea and finalized the manuscript. All authors read and approved the final manuscript.

Conflict of interest The authors declare that they have no conflict of interest.

Supplementary information Supporting data are available in the online version of the paper.

Kaiyuan Zhang received his PhD degree in inorganic chemistry from Shandong University in 2021. Then, he works at the School of Chemistry and Chemical Engineering, Linyi University. His research focuses on developing Si/SiO_x-based anode materials for lithium-ion batteries.

Xin Gu received his PhD degree in inorganic chemistry from Shandong University in 2014. After his postdoctoral research at the College of Science, China University of Petroleum (East China), he joined the College of New Energy, China University of Petroleum (East China). He is currently an associate professor. His work mainly focuses on the exploration of electrode materials for rechargeable batteries.

Zhao Qian received his PhD degree from KTH Royal Institute of Technology (Sweden) in 2013. After his postdoctoral research at Uppsala University (Sweden), he joined Shandong University (China). He is currently a full-time professor in materials science and engineering and mainly conducts research on computational materials science (DFT, First-principles, etc.) and electronic structure calculations/explorations.

Jian Yang received his BSc and PhD degrees from the University of Science and Technology of China. He joined the School of Chemistry and Chemical Engineering, Shandong University in 2011. His research interests focus on the development of new electrode materials for Na/Zn ion batteries, unraveling the underlying electrochemical reactions, and designing electrolyte additives/polymers for advanced batteries.

氮掺杂$Ti_3C_2T_x$ MXene纳米片包覆的SiO_x实现储锂性能提升

张开元[1], 赵丹[2], 钱钊[2*], 顾鑫[3*], 杨剑[1*], 钱逸泰[1,4]

摘要 构建具有快速反应动力学和优异循环稳定性的SiO_x基负极材料是获取高性能锂离子电池的关键和挑战. 本文中, 我们利用三聚氰胺辅助的球磨和退火方法, 合成了氮掺杂的$Ti_3C_2T_x$ MXene超薄片层(NTS)包覆的SiO_x复合材料. 通过对比实验和理论计算, 我们论证了三聚氰胺剥离MXene的作用机理. SiO_x与NTS之间强烈的界面相互作用(Si–O–Ti键)可以有效地增强电子转移, 确保电极的稳定性. 此外, 具有丰富表面基团的NTS使复合材料具有赝电容性能, 有利于快速储锂. 因此, 该复合材料展现出了长循环寿命(在1.0 A g^{-1}的电流密度下, 循环800次后比容量保持为~700 mA h g^{-1})和优越的倍率性能(在5 A g^{-1}的电流密度下, 比容量为596.4 mA h g^{-1}). 更重要的是, 在高负载量下, 该复合材料在半电池和全电池中均表现出较高的面积比容量和良好的循环稳定性, 展现出了良好的应用潜力.

